


Enhancing flat plate collector efficiency with microtubes and sodium sulfate decahydrate-copper oxide PCM

Muhammad Shehram , Muhammad Najwan Hamidi*, Aeizal Azman Abdul Wahab, and Mohd Khairunaz Mat Desa

School of Electrical and Electronic Engineering, Universiti Sains Malaysia, Engineering Campus, 14300 Nibong Tebal, Pulau Pinang, Malaysia

Received: 12 January 2024 / Accepted: 29 October 2025

Abstract. Thermal energy storage not only conserves energy but also addresses the demand for renewable energy sources. Phase Change Materials (PCM) play a crucial role in storing solar thermal heat, thanks to their high heat of fusion and thermal conductivity. Incorporating PCMs has enhanced the performance of Flat Plate Collectors (FPCs). This particular design utilizes sodium sulfate decahydrate and copper oxide-based inorganic PCMs to effectively store thermal energy. The integration of this PCM with an FPC featuring microtubes has proven highly effective. The use of salt hydrate-based PCMs resulted in a notable 15% improvement in the efficiency of FPCs. Additionally, there is an enhancement in the storage time of thermal heat. To mitigate tube corrosion, copper oxide was introduced alongside sodium sulfate decahydrate. Simulation results were obtained across various Reynolds number values ranging from 1500 to 4000. Mathematical modeling and simulation were employed to assess thermal heat transfer, fluid dynamics, and heat loss. The simulation outcomes indicate a substantial improvement in the FPC's efficiency, reaching up to 85%, attributed to the incorporation of PCM for heat storage.

Keywords: FPCs, Thermal energy storage, Nanotubes, Inorganic PCM, Thermal heat loss, Efficiency improvement.

Abbreviations

A_c	Area of collector	L_e	Side insulations loss
Q_u	Overall heat transfer in flat plate	$h_{e,a}$	Heat coefficient of collector in side
F_r	Fractional efficiency	R_{pc}	Overall heat transfer coefficient
G_t	Solar constant	R_{ca}	Resistance of glass cover and surrounding
α_t	Transmissivity of the glass	h_{pc}	Convection heat coefficient of absorber
U_L	Overall heat loss	σ	Boltzmann constant
T_{in}	Input temperature in flat plate	T_{pm}	Mean temperature of collector
T_{out}	Output temperature	T_c	Glass cover temperature
T_i	Inlet temperature in PCM	ϵ_p	Absorber plate emissivity
m	Mass of the working fluid	ϵ_c	Glass cover emissivity
c_p	Specific heat capacity of heat transfer fluid	h_w	Wind heat transfer coefficient
U_t	Top heat loss in collector	T_s	Sky temperature effects
U_b	Bottom heat loss collector	T_a	Ambient temperature
U_e	Side heat loss in collector	η_{th}	Thermal efficiency of collector
L_b	Insulation thickness	$dT_{p,avg}$	Average temperature of the phase change
K_b	Insulation thermal conductivity	d_t	Diameter of the tubes
$h_{b,a}$	Convection heat loss of collector at bottom	Q_{ch}	Charging of the PCMs
		η_0	Output efficiency of collector
		I	Irradiance
		Q_{dis}	Discharging of the PCMs
		T_{pcm}	Temperature of PCM

* Corresponding author: najwan@usm.my

R_{tot}	Total resistance loss
A_{pcm}	Area of PCM occupy
η_{ch}	Efficiency of PCMs charging
η_{dis}	Efficiency of PCMs during discharging
$E_{\text{x,stored}}$	Total exergy stored
$E_{\text{x,in}}$	Inlet exergy
$E_{\text{x,out}}$	Output exergy during discharging
$\ln\left(\frac{T_{\text{in}}}{T_{\text{out}}}\right)$	PCM total input and output temperature
PCM	Phase Change Material

1 Introduction

Enhancing the efficiency of renewable energy systems has become a prevailing trend in the current era, aiming to diminish reliance on fossil fuels and promote the generation of clean energy. Renewable energy resources stand out as environmentally friendly alternatives, contributing to the mitigation of global warming. Among these, Flat Plate Collectors (FPCs) emerge as a robust source in the field of solar thermal energy. Operating effectively at both high and moderate temperatures, FPCs adeptly absorb both beam and diffused sunlight. FPC has versatile applications in renewable energy, serving purposes such as heating and cooling. Despite their advantages, a significant challenge lies in the intermittent availability of renewable energy resources like solar power, which is contingent upon specific times of the day. Thermal energy storage emerges as a pivotal solution to address this temporal limitation, ensuring a more consistent and reliable supply of energy [1–3].

In [4], a latent heat thermal energy storage system is employed to store thermal energy within Phase Change Materials (PCMs). This thermal energy storage method plays a crucial role in shifting load demand and finds application in diverse areas such as air-conditioning and heat recovery. Notably, latent heat storage is recognized for its capacity to store high levels of thermal energy. In comparison to sensible heat storage, latent heat storage exhibits a remarkable advantage, storing thermal energy at a rate 3–4 times higher per unit volume. Addressing thermal heat storage is a primary consideration when utilizing a system for storing heat for future use. Initially, water is employed as a medium to store thermal heat, and subsequently, phase-change materials are introduced to enhance the storage capacity. In the charging process, the PCM undergoes a transition from a solid to a liquid state, effectively storing thermal heat. During the discharging process, the stored heat is released and harnessed to power various applications. This cyclical process facilitates the efficient utilization of stored thermal energy for practical purposes [5].

In [6], it is noted that PCMs exhibit a sustained high thermal energy density even at low temperatures. This stored thermal energy proves valuable for cooling applications. The system utilizes salt-based PCMs with a melting temperature set at 142 °C to store the thermal energy. Thermal oil serves as the working fluid for the collection of thermal heat, which is then stored in sodium-based salts.

The simulation of this system is carried out using TRNSYS, providing a comprehensive analysis of its performance and efficiency. Nanoparticles are added with the PCMs to produce a nanocomposite to improve thermo-physical properties of the PCMs [7]. In the system described, triple-PCMs featuring distinct melting point temperatures (63 °C, 54 °C, and 43 °C) are employed to effectively store thermal heat energy. This innovative approach involves storing PCM within triple concentric tubes. The thermal heat is stored through a latent heat process, wherein both the transfer of heat and the storage of heat in the PCM contribute to the overall efficiency of the system. This design optimizes the utilization of latent heat for thermal energy storage [8].

In [9, 10], the investigation focuses on enhancing the performance of FPCs through the incorporation of PCMs and helically corrugated heat-collecting tubes. The results reveal a significant improvement in the efficiency of the FPC, with a notable decrease in heat loss by 39.8%, as indicated by the output working fluid temperature difference. Specifically, the use of PCMs contributes to a remarkable efficiency boost, ranging from 41.5% to 48.9% for the FPC. This underscores the positive impact of integrating PCMs and innovative tube designs on overall collector performance. In [11], a nano-based PCM is employed for thermal energy storage, utilizing three distinct nano PCMs. The study reveals that the charging and discharging efficiency of the PCM system is significantly improved, specifically by 24%–28%, through the use of amino-functional PCMs. This signifies a notable advancement in the effectiveness of the thermal energy storage process, highlighting the positive impact of incorporating amino-functional PCMs in enhancing both charging and discharging efficiency.

A novel heat storage tank, outlined in [12, 13], has been developed to capture and store heat from PCMs, alongside water collection. The tank can store this heat within a span of 2 h. The performance of the tank loaded with PCMs shows a 10% improvement over the non-loaded PCM tank. The enhanced heat transfer efficiency of the collector can be attributed to the presence of PCMs. In [14], a novel supercooled PCM is introduced, designed to enhance the efficiency of flat-type solar collectors to 15%. The supercooled PCM has a melting point of 323.15 K, and it operates with a cooling temperature of 30 K, resulting in a 15% increase in the cooling rate. In [15], various types of PCMs are tested to evaluate their compatibility with highly efficient energy storage applications. A small-scale prototype system is designed to assess the suitability of PCM for such energy storage materials.

Abu-Hamdeh *et al.* [16] describes a method where thermal energy is stored in PCM to meet the energy demands for both heating and cooling loads in a building. The thermal heat is collected through the use of an FPC. The PCM employed in this context consists of paraffin wax combined with graphene or graphene oxide-based materials. This incorporation enhances the efficiency of the FPC and extends the storage time for thermal energy. In [17], PCMs designed for low-temperature thermal heat energy storage are introduced. These materials are engineered to absorb energy at the lowest temperatures and release it when needed at similarly low values. The document delves into

the details of thermal energy storage and management associated with these low-temperature-based PCMs. In [18], the enhancement of thermal properties in PCMs is explored by altering the size and shape of the PCM storage container. The thermal energy storage capacity is improved by increasing the storage area, as discussed in the study.

In [19], thermal heat is stored using paraffin wax, and an FPC is employed to gather this heat. This stored heat becomes valuable during periods of insufficient solar radiation intensity. The incorporation of PCMs enhances the output of heat storage by 15%. In [20], the presence of PCMs results in a temperature difference that is 2 °C–9 °C higher compared to a basic FPC without such materials. The collector's efficiency is notably improved with the incorporation of PCMs. In [21], the thermal stability of heat storage is enhanced by incorporating nanoparticles of inorganic materials along with PCMs. The efficiency is further elevated by utilizing rotating tubes within the FPC. Specifically, 3% iron-oxide nanoparticles are introduced into the PCM.

In [22], the collector's efficiency experiences a notable 15% improvement through the introduction of alumina nanoparticles combined with PCMs. These PCMs not only facilitate the cooling of the collector but also serve the additional function of acting as a super cooler. In [23], sodium dodecyl sulfate serves as a PCM for the storage of thermal energy in conjunction with multiwall carbon nanotubes. The study employs a nanocomposite material consisting of polyethylene glycol 8,000 with varying mass fractions (0%, 0.5%, 1%, 2%, and 5%) to augment its performance. In [24], a graphene-based aerogel is employed to mitigate the leakage behavior of tubes containing PCMs. The approach involves the use of graphene oxide-based nanosheets to coat carbon-based nanotubes, resulting in an enhancement of the heating and cooling efficiency by up to 93.44%. In [25], tetradecane is utilized as the PCM, and the efficiency is augmented by incorporating porous nano carbon tubes. Figure 1 shows the FPC integrated with PCMs.

Paraffin wax PCMs combined with three types of nanoparticles, namely metal foams and wavy fin-based FPCs, aim to improve the performance of FPCs. Various weight percentages of nanoparticles are incorporated into the PCM to enhance its efficiency. Specifically, aluminum foam nanoparticles are used at weight percentages of 0.92%, 0.95%, and 5% in conjunction with the collector. During sunlight exposure, this PCM stores energy, which can then be utilized when solar radiation is unavailable [26].

The double-pipe heat exchanger is integrated into the FPC to improve its performance. The geometry of the collector pipes plays a crucial role in enhancing efficiency. Utilizing a lobes-type geometry reduces melting time by 18.32%, thereby boosting collector performance. Additionally, various foam materials are incorporated with the PCM to further enhance the collector's efficiency [27].

A triple-tube heat exchanger pipe is employed in the FPC to enhance its performance significantly. This design reduces the melting rate of PCM and NePCM by 11%–12%, facilitated by the use of internal and external fins. Furthermore, the addition of alumina increases the

thermal conductivity of the PCM by 0.2 W/m K, further improving overall efficiency [28].

In this research, the efficacy of the FPC is enhanced through the incorporation of PCMs. Carbon-based nanotubes are employed, serving as vessels for the PCMs, allowing them to efficiently gather thermal heat and store thermal energy. The integration of inorganic-based PCMs, particularly sodium sulfate decahydrate, is a noteworthy aspect of the design. This specific salt is chosen for its superior thermal conductivity and substantial thermal energy storage capacity. To address potential corrosion effects on the tubes, copper-oxide-based nanocomposite materials are introduced alongside the inorganic salts. This addition aims to mitigate corrosion and enhance the durability of the system. The efficiency of the FPCs is assessed by testing the temperature of the working fluid at various Reynolds (Re) numbers, providing insights into the overall performance of the design.

2 Methodology

2.1 FPC integrated with PCM

An FPC serves as a mechanism for converting solar thermal energy into a practical and usable form. This involves the utilization of PCMs integrated within the collector to store the thermal energy derived from the sun. The stored heat becomes instrumental during periods when sunlight is unavailable, such as during nighttime or on rainy days. In these instances, the stored heat is employed to power the connected load, compensating for the decreased performance of the FPC.

The applications of this stored heat are diverse and include driving cooling systems, meeting hot water requirements, and facilitating drying processes [29]. The FPC consists of four key components: Absorber plates, glass, insulation, and working fluids. Absorber plates play a crucial role in absorbing the sun's intense radiation and transforming it into a usable and efficient form of energy.

Figure 2 illustrates the integration of PCMs with an FPC using nanotubes, with the PCM housed within these carbon-based tubes. To ensure leak-free containment of the PCM, graphene gel is applied. This setup allows the storage of solar thermal energy in the tubes when sunlight is available, and the accumulated energy serves the purpose of providing heat during nighttime periods. As an additional protective measure against corrosion of the tubes, nanocomposite materials based on copper oxide are introduced into the PCM. This integration enhances the durability and longevity of the system, contributing to its overall efficiency and performance.

2.2 Nanotubes construction and performance in FPC

In this design, carbon-based nanotubes play a crucial role in extending the thermal heat storage duration and enhancing the overall efficiency of the FPC. The thermal energy of the collector is stored using a salt-based PCM. To mitigate corrosion and further optimize thermal heat storage,

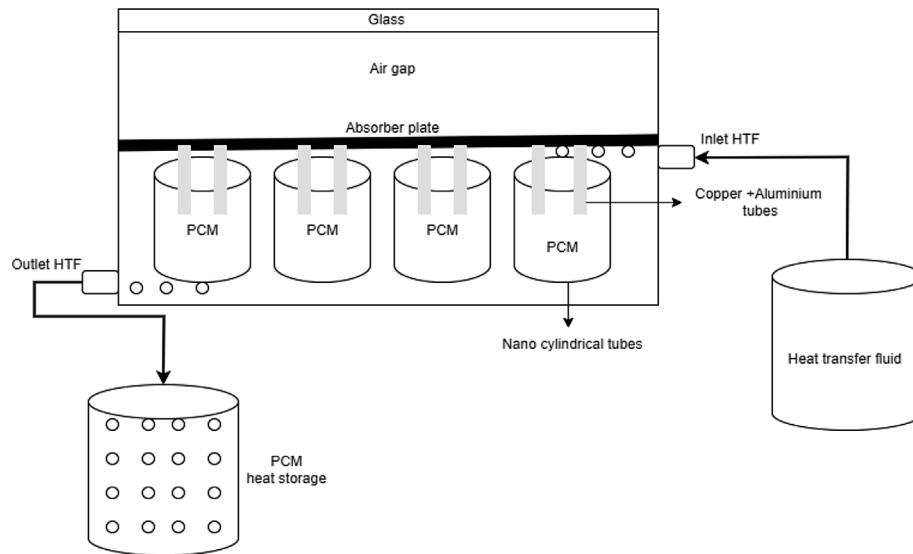


Fig. 1. PCMs integrated with FPC.

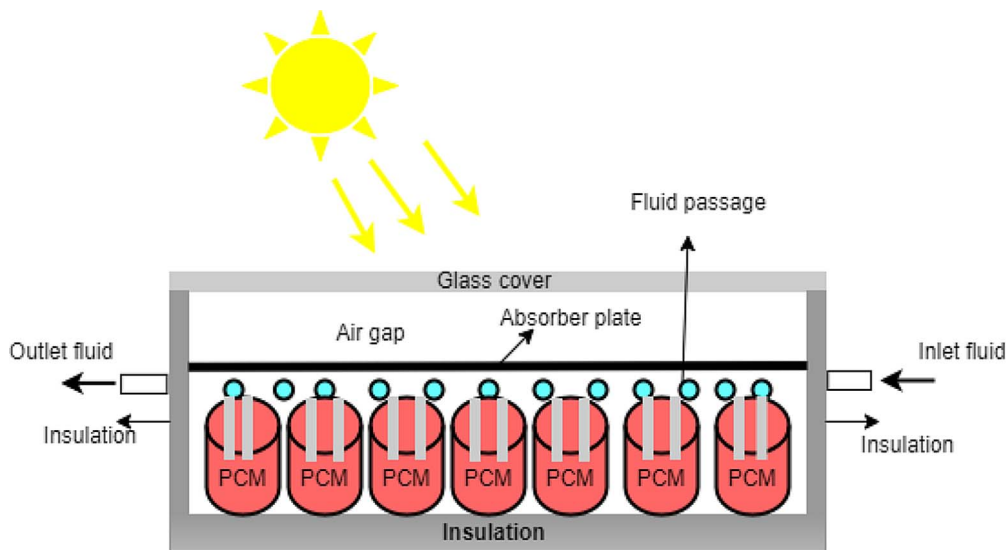


Fig. 2. FPC with integration of the PCMs in nanotubes.

nanocomposite materials with a copper oxide base are introduced into the PCM. This addition not only prevents corrosion but also contributes to prolonging the storage time of thermal heat.

Figure 3 illustrates the configuration of carbon-based nanotubes integrating phase-change materials within the FPC design. The thermal conductivity of the multiwall nanotubes, being carbon-based, is notably efficient [30]. Within these tubes, the PCM is housed, featuring a hollow middle section. The heat transfer fluid circulates through this central space on both sides of the multiwall nanotubes.

To prevent corrosion, a copper insulation layer is strategically positioned between the passage of heat transfer fluid and the tubes containing PCM. When sunlight is present, the absorber plate captures thermal heat and transfers it to the working fluids. These fluids accumulate the heat,

with a portion directed towards the PCM for storage. The remaining thermal energy is then transferred to the load. To enhance thermal stability, nanocomposite materials are added in limited amounts, specifically up to 0.05%. This addition improves the PCM's thermal stability by up to 30%. The stored heat serves as a valuable resource for subsequent use, particularly during periods of inconsistent sunlight, such as rainy days, stabilizing the load requirements by utilizing the stored energy.

2.3 Classification of PCMs

Utilizing thermal energy storage emerges as the optimal solution to address energy crises and meet the growing demand for energy in buildings and various industrial applications. Among the available options, PCMs stand out as

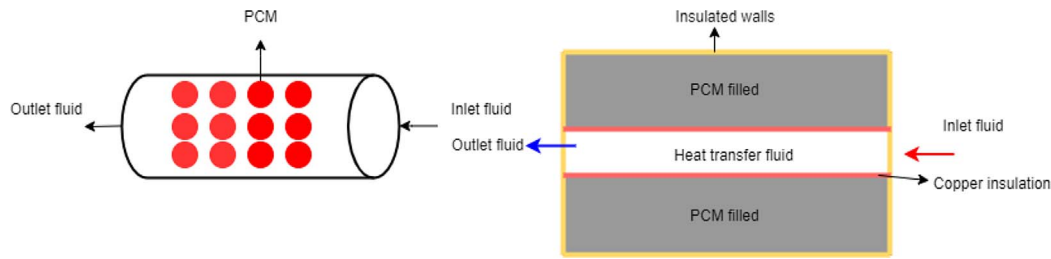


Fig. 3. Nanotubes construction and process of PCMs energy storage.

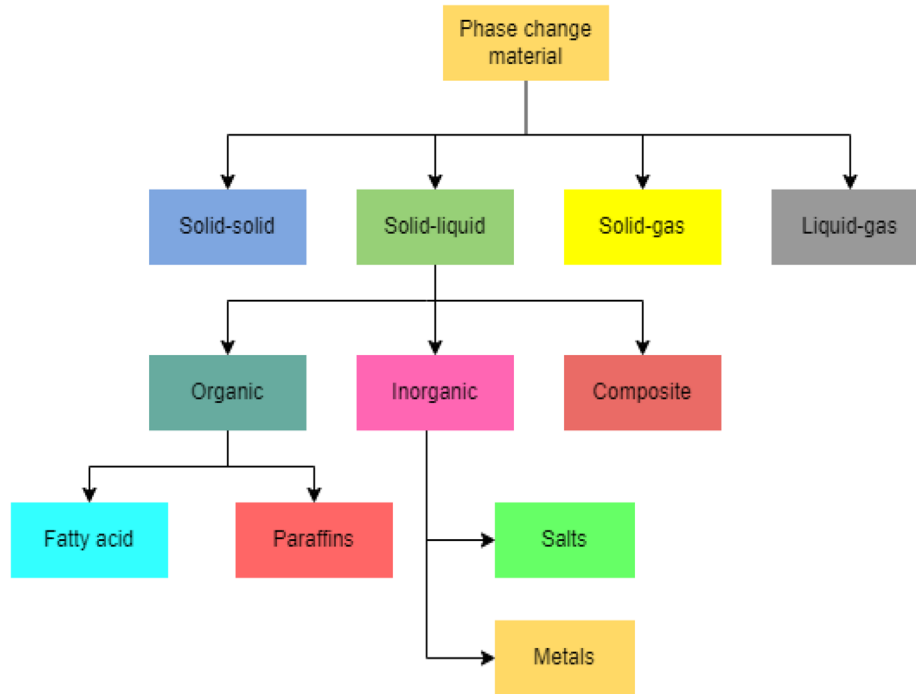


Fig. 4. Classification of the PCMs [32].

the most efficient choice for storing thermal energy. These materials excel in absorbing and retaining substantial amounts of energy over extended periods [31].

Figure 4 illustrates the categorization of PCMs according to their material properties and availability. These materials are divided into four sub-categories based on their phase transition: Solid–solid, solid–liquid, liquid–gas, and solid–gas. The liquid–gas and solid–gas forms, however, are deemed impractical due to the significant space they occupy. The prevalent choice among PCMs is the solid–liquid category, with organic and inorganic types being the primary classifications [32]. In the proposed design, the utilization of inorganic-based PCMs is advocated for storing the thermal heat generated by FPCs.

2.4 Inorganic-based PCMs

Inorganic PCMs typically comprise metallic salts and salt hydrates for the storage of thermal heat. In this particular configuration, PCMs based on salt hydrates are employed

to capture the thermal energy within the FPC. Within salt hydrates, ion-dipole forces in the PCM create connections between the two hydrogen bonds [33]. Weak forces of attraction exist among water molecules, and when latent heat energy is absorbed, these forces break. This results in the dissolution of the water molecule, and sodium sulfate begins to store thermal energy. The latent heat is generated as the salt initiates the hydration/dehydration process.

Figure 5 illustrates the phase transition of the PCM, depicting the absorption and release of latent heat of fusion. In this configuration, sodium sulfate decahydrate salt is employed for energy storage. Initially, during the first stage, the salt is in a solid form. When solar radiation is present, the absorber plate collects thermal heat and channels it to the PCM, initiating the phase transition. The salt absorbs and stores this heat in the form of latent heat. In the subsequent stage, when sunlight is unavailable, the stored heat begins to release, facilitating the operation of the load. As the entire energy is discharged, the PCM solidifies completely.

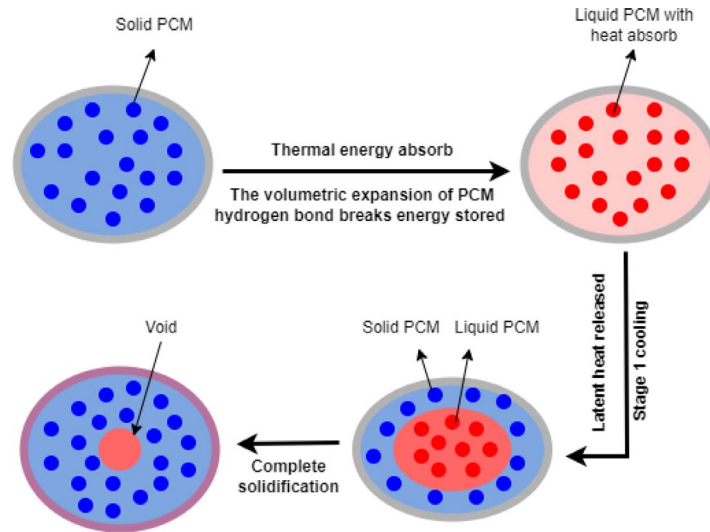


Fig. 5. PCMs transition from solid to liquid and liquid to solid.

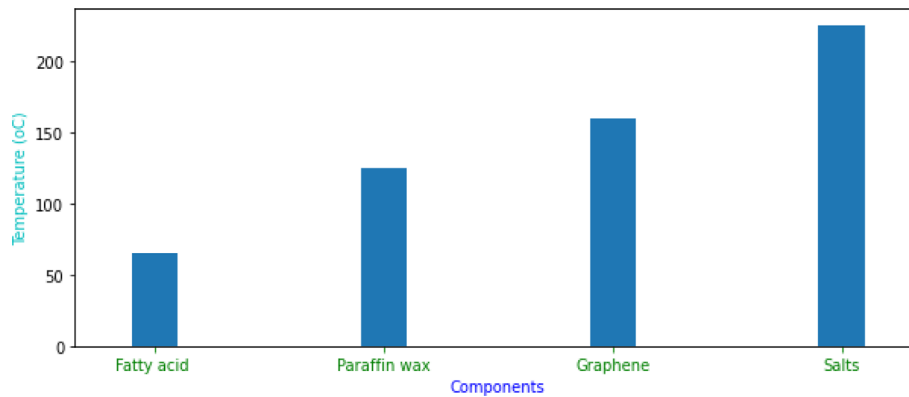


Fig. 6. Melting points of different PCMs [34, 35].

Sodium sulfate decahydrate exhibits commendable thermal conductivity, making it effective for heat transfer, and it possesses a high temperature release capability. The introduction of nanocomposite materials serves to augment the thermal stability of these salts, thereby enhancing their capacity for bearing and transmitting heat [34].

Figure 6 provides a comprehensive overview of the melting points and heat-bearing capacities of various common PCMs. Fatty acid-based PCMs exhibit a melting point of 65 °C, while paraffin wax surpasses this with a melting point of 125 °C. Salts, on the other hand, boast the highest melting point at 225 °C. The PCMs based on salts are particularly advantageous for thermal heat storage, given their elevated melting points and superior thermal conductivity [35].

2.5 Copper oxide-based nanocomposite material added with PCM

Nanocomposite materials undergo supplementation with PCMs to improve their thermal conductivity. Typically, two categories of materials, organic and inorganic

composites, are employed for this purpose [35]. In terms of thermal conductivity, inorganic-based composite materials outperform their organic counterparts. Among inorganic composite materials, metals and metal alloys are frequently utilized due to their high heat-bearing capacity [36]. In the proposed system, copper oxide composite material is introduced to augment the thermal stability of sodium sulfate decahydrate salt.

In Figure 7a, the illustration depicts the preparation of nanocomposite materials incorporating PCMs, specifically sodium sulfate decahydrate salts. To enhance the thermal conductivity of the PCMs, copper oxide is introduced along with the sodium sulfate salt. Furthermore, the inclusion of copper serves the dual purpose of enhancing thermal conductivity and providing corrosion protection for the microtubes in the FPCs.

In Figure 7b, the illustration showcases the varieties of nanocomposite materials suitable for incorporation with phase change. Two prevalent types are organic and inorganic. In the scope of inorganic materials, metals and metalloids find common application, whereas organic materials typically involve the use of graphite, carbon nanotubes, and

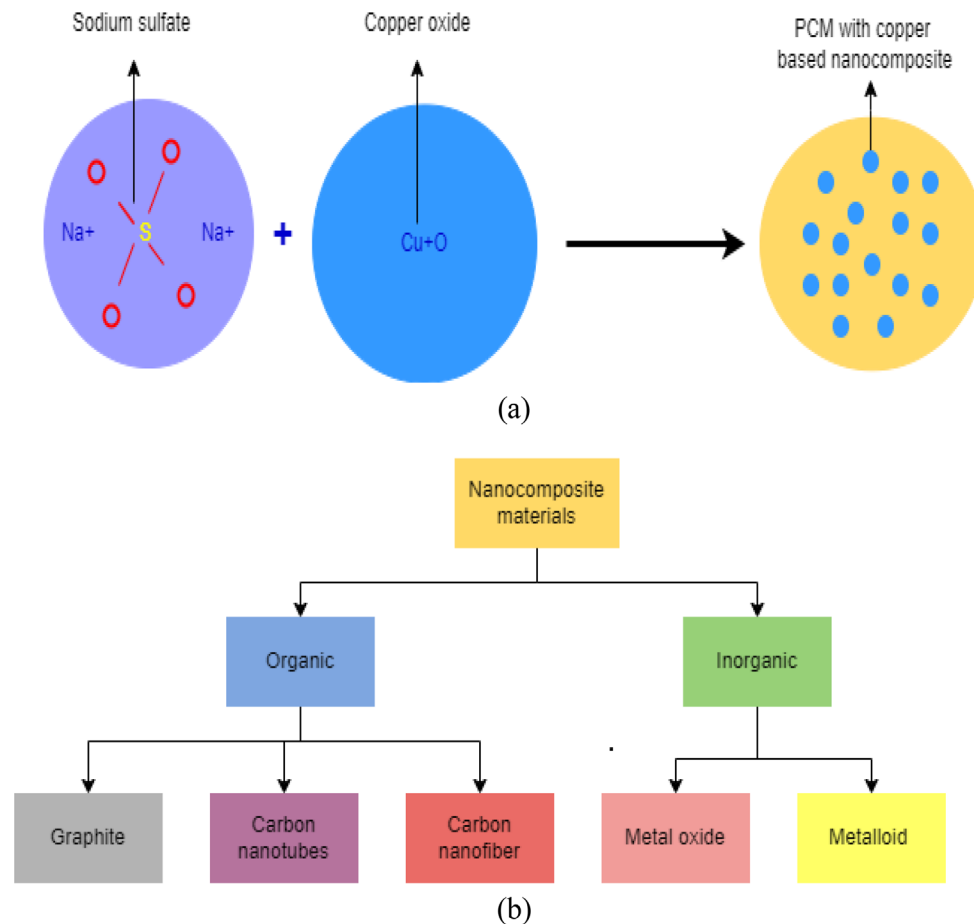


Fig. 7. (a) PCM preparation with copper oxide nanocomposite (b) Nanocomposite material types.

carbon nanofibers to augment the thermal stability of thermal heat storage. The elevated melting points and heat-bearing capacity of inorganic materials, in comparison to organic counterparts, result from the robust bonding between molecules in metals. Ionic, covalent, or coordinate covalent bonding exists, necessitating more energy for molecule breaking.

2.6 Thermal heat storage categories for PCMs

There are two main categories of thermal energy storage: Sensible heat storage and latent heat storage. Latent heat storage exhibits a higher thermal energy storage capacity per unit volume when compared to sensible heat storage [37].

Figure 8 illustrates the thermal energy storage categories specific to PCMs. The process of adding or removing heat in PCMs is indicative of sensible heat, while the energy needed to alter the shape or state of materials is termed the latent heat stage. Sensible heat storage materials include water and rocks, whereas organic and inorganic materials serve as latent heat storage materials. In this particular design, latent heat storage materials are employed for the storage of thermal energy.

PCMs undergo a transition between solid and liquid or solid and gas states through processes such as melting or

freezing. When the temperature rises, these materials, known as PCMs, store energy. During this phase, the molecules of the PCM begin to break, initiating an endothermic process in which the PCM absorbs energy. In the absence of heat, the PCM starts discharging, releasing stored energy and transitioning from its liquid state to a solid form in an exothermic reaction. This charging and discharging cycle of phase-change materials occurs with a minimal change in volume fraction, typically less than 10% [38].

3 Mathematical modeling

3.1 Assumptions

This study investigates the integration of NePCM into an FPC to enhance its thermal performance. The analysis encompasses heat-loss comparisons (with and without NePCM), output temperature variations during NePCM charging and discharging, heat transfer rates, and melting fraction rates. Energy balance equations and boundary conditions are formulated for both heat transfer fluids. Key assumptions for this study include:

- The Reynolds number for the heat transfer fluid is maintained between 1,500 and 4,000.

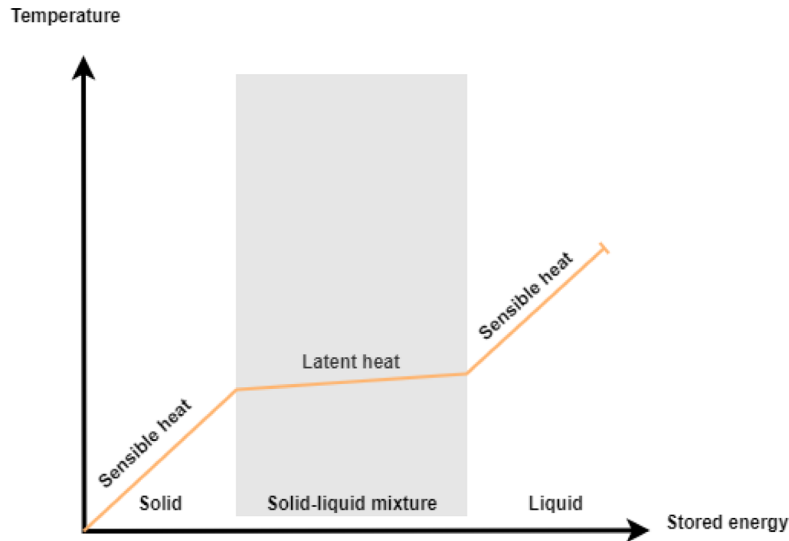


Fig. 8. Thermal energy storage categories in PCM.

- The use of highly conductive copper and aluminum for the heat transfer fluid tubes results in negligible thermal resistance between the NePCM and the heat transfer fluid.
- The full insulation of the PCM storage tank's outer layer results in negligible heat loss from the outer surface.
- Unlike the heat transfer fluid, whose properties remain constant regardless of temperature, the NePCM used in this study exhibits properties that vary with the temperature of the FPC.
- The collector experiences inlet and outlet temperatures ranging from 26 °C to 70 °C during peak hours.
- During charging, the NePCM completely transitions from solid to liquid, achieving a melting fraction of 1, which signifies maximum energy storage efficiency.
- The liquid NePCM is characterized by laminar flow, incompressibility, unsteady state, and Newtonian flow behavior.
- Nanomaterials like copper oxide are evenly distributed within the PCM, where $\nabla \cdot U = 0$.
- The study assumes a no-slip boundary condition, meaning the fluid velocity at the walls is zero.

3.2 Thermo-physical properties and boundary conditions

Table 1 presents the thermo-physical properties of the PCM and metal oxide used in this study. It includes specific heat capacity, melting and solidification temperatures, density, thermal conductivity, latent heat, dynamic viscosity, and thermal expansion volume for both the PCM and metal oxide.

Table 2 outlines the boundary conditions for the NePCM in this study, detailing the melting and solidification processes. The velocity of the NePCM is 4.6 during melting and 1.4 during solidification, with a turbulence

intensity of 5 for both processes. The melting temperature of the NePCM is 65 °C, solidification occurs at 15 °C, and the pressure outlet is set at 0.3. Fluid flow rates are specified as 15 and 9 for different conditions.

3.3 Analytical model of heat transfer in nanoparticles of NePCM

The application of NePCM involves multiple cycles of charging and discharging over an extended period. Heat transfer within the NePCM occurs through sedimentation, Brownian diffusion, and thermophoresis diffusion of the nanoparticles, which are non-homogeneously distributed throughout the PCM. In this study, an aluminum copper pipe is used to transfer heat through diffusion. The analytical modeling of the system is outlined as follows. First, the density and specific heat capacity of the NePCM used in this work are determined. Then, using the provided equations, the latent heat value, thermal expansion, dynamic viscosity, thermal conductivity, and melting fraction of the NePCM are calculated. The equations in Table 3 are used to determine the energy balance and energy transfer in the nanoparticles of the NePCM. These equations illustrate the continuity value, momentum, energy, liquid fraction, buoyancy term, and momentum sources of the NePCM. Here, u , t , T , P , and g depict the velocity vector, time, temperature, pressure, and gravity, respectively. Where μ_m is dynamic viscosity, ρ_m is density, C_{pm} is specific heat capacity, k_m is thermal conductivity, and β_m is volumetric expansion coefficient. S_m is the momentum source term, Sh is the enthalpy source term, T_l is liquid temperature, T_s is solid temperature, T_{me} is melting temperature, and C and b are constants with a value of 1.6×10^6 . The term g_k represents the Boussinesq gravity term.

Equation (1) determines the density of the NePCM, while equation (2) determines the specific heat capacity of the NePCM, where ρ represents the density of the materials, ϕ is the nano-additive volume fraction, and ρ_{NM} is the density of nanomaterials [41–43]:

Table 1. Thermo-physical properties of the PCM and metal oxide used in this work.

Properties	Sodium sulfate decahydrate	Copper oxide
Specific heat capacity J/kg-K	128.2	42.3
Melting and solidification °C	32.4/16.4	1326/
Density g/m ³	1.46	6.315
Thermal conductivity W/m.K	1.02	32.9
Latent heat J/g	208.2	148.30
Dynamic viscosity mPa-s	2.48	11.8
Thermal expansion volume [K ⁻¹]	4.2–300	298.15–1300

Table 2. Boundary conditions of the PCM in this work.

Boundary condition	Melting	Solidification
Velocity (m/S)	4.3	1.4
Turbulence intensity at inlet %	5	5
Inlet fluid temperature	65	15
Pressure outlet (atm)	0.3	0.3
Mass flow rate m(kg/s)	0.2–15	0.2–9

Table 3. Nanoparticles in PCM energy balance and transfer equations [39, 40].

Component	Equations
Continuity	$\nabla \cdot u = 0$
Momentum	$\frac{\partial u}{\partial t} + \nabla \cdot (uu) = -\nabla \left(\frac{P}{\rho_m} \right) + \nabla \left(\frac{\mu_m}{\rho_m} \nabla u \right) + g_k + S_m$
Energy	$\frac{\partial T}{\partial t} + \nabla \cdot (Tu) = \nabla \cdot \left(\frac{k_m}{\rho_m c_{pm}} \nabla T \right) + S_h - \nabla \cdot q_t$
Liquid fraction	$\alpha = 0.5 \cdot \text{erf} \left(\frac{4(T - T_{me})}{T_l - T_s} \right) + 0.5$
Buoyancy terms	$g_k = [1 - \beta_m (T - T_{ref})]g$
Momentum source	$S_m = -uC \frac{(1 - \alpha)^2}{\alpha^3 + b}$

$$\rho_{\text{NePCM}} = (1 - \varphi)\rho_{\text{PCM}}\varphi\rho_{\text{NM}}, \quad (1)$$

$$(\rho C_p)_{\text{NePCM}} = (1 - \varphi)(\rho C_p)_{\text{PCM}} + \varphi(\rho C_p)_{\text{NM}}. \quad (2)$$

Equation (3) is used to determine the latent heat of the NePCM, where L represents the latent heat of the materials used in the NePCM.

$$(\rho L)_{\text{NePCM}} = (1 - \varphi)(\rho L)_{\text{PCM}}. \quad (3)$$

Equation (4) is used to determine the thermal expansion of the NePCM, where β represents the coefficient of thermal expansion:

$$(\rho\beta)_{\text{NePCM}} = (1 - \varphi)(\rho\beta)_{\text{PCM}}. \quad (4)$$

Equation (5) is used to determine the dynamic viscosity of the NePCM, where μ represents the dynamic viscosity:

$$\mu_{\text{NePCM}} = 0.9197e^{22.8539\varphi}\mu_{\text{PCM}}. \quad (5)$$

Equation (6) is used to determine the thermal conductivity of the NePCM, where k_{NP} is the thermal conductivity of the nanomaterial and k_{PCM} is the thermal conductivity of the PCM.

$$k_{\text{NePCM}} = k_{\text{PCM}} \left[\frac{k_{\text{NP}} + 2k_{\text{pcm}} - 2\varphi(k_{\text{PCM}} - k_{\text{NP}})}{k_{\text{NP}} + 2k_{\text{PCM}} + \varphi(k_{\text{pcm}} - k_{\text{NP}})} \right] \quad (6)$$

Equation (7) is used to determine the melting point of the NePCM, where $T_{m,l}$ and $T_{m,u}$ are the lower and upper temperature point values, respectively.

$$\varphi = \begin{cases} \frac{T - T_{m,l}}{T_{m,u} - T_{m,l}}, & 0 < T < T_{m,l} \\ T_{m,l} \leq T \leq T_{m,u} \\ 1 & T > T_{m,u} \end{cases} \quad (7)$$

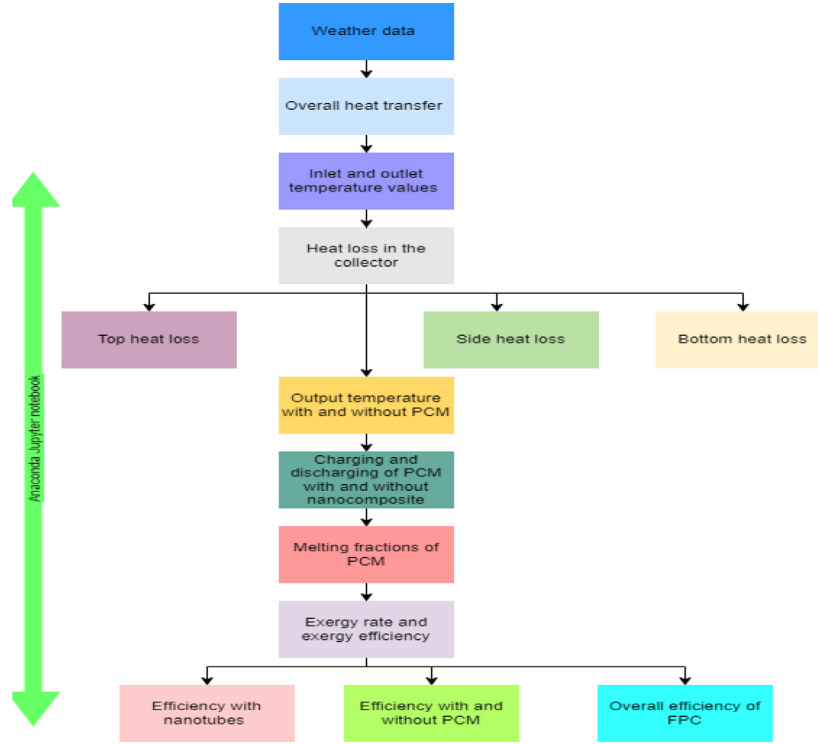


Fig. 9. Mathematical modeling flow chart for simulation.

The FPC undergoes mathematical modeling by incorporating PCMs, with the addition of nanocomposite materials to augment the thermal storage capacity of these PCMs. Several steps have been implemented to assess the efficiency of the FPC featuring PCMs shown in **Figure 9**. Initially, the total heat transfer of the FPC is quantified, followed by the determination of its total heat loss. Subsequently, the overall efficiency of the FPC is calculated. Finally, the charging and discharging processes of the PCMs are investigated [11, 35, 44].

Equation (8) is used to determine the total heat transfer of the FPCs, where Q_u represents the overall heat transfer of the FPC, A_c is the area of the collector, F_r is the fractional efficiency of the collector, G_t is the solar constant value, α_t is the transmissivity of the glass, U_L is the overall heat loss coefficient of the FPC, T_{in} is the inlet temperature, T_i is the inlet temperature during phase change, m is the mass of the fluid, c_p is the specific heat capacity of the heat transfer fluid, and T_{out} is the outlet temperature of the collector.

$$\begin{aligned} Q_u &= A_c F_r [G_t \alpha_t - U_L (T_{in} - T_i)] \\ &= m c_p (T_{in} - T_{out}). \end{aligned} \quad (8)$$

Equation (9) is used to determine the overall heat loss of the FPCs. U_L , the overall heat loss coefficient, is separated into: U_t , representing the top heat loss; U_b , representing the bottom heat loss; and U_e , also representing the side loss of the FPC.

$$U_L = U_t + U_b + U_e. \quad (9)$$

The bottom heat loss coefficient (U_b) of an FPC, as shown in equation (10), is determined by the combined effects of conduction through the insulation and convection to the surrounding air. The conduction component is governed by the insulation thickness (L_b) and its thermal conductivity (K_b), while the convective heat loss is represented by $h_{b,a}$.

$$U_b = \left(\frac{L_b}{K_b} + \frac{1}{h_{b,a}} \right). \quad (10)$$

The side heat loss coefficient (U_e) of the FPC, as shown in equation (11), is determined by the combined effects of conduction through the side insulation and convection to the surrounding air. The conduction component is governed by the insulation thickness (L_e), while the convective heat loss is represented by $h_{e,a}$.

$$U_e = \left(\frac{L_e}{K_b} + \frac{1}{h_{e,a}} \right) \quad (11)$$

The top heat loss coefficient (U_t) of the collector, as shown in equation (12), is determined by the combined effects of the overall heat transfer coefficient between the absorber plate and the glass cover (R_{pc}) and the thermal resistance between the glass cover and the surrounding environment (R_{ca}).

$$U_t = \frac{1}{R_{pc}} + \frac{1}{R_{ca}}. \quad (12)$$

In equation (13), R_{pc} represents the overall heat transfer coefficient, which combines the radiative and convective

heat transfer between the absorber plate and the glass cover. The convective component, h_{pc} , depends on several factors, including the Stefan-Boltzmann constant (σ), the mean temperature of the collector (T_{pm}), the glass cover temperature (T_c), and the emissivity of the absorber plate (ϵ_p) and glass cover (ϵ_c).

$$R_{pc} = \left[h_{pc} + \frac{\sigma(T_{pm}+T_c)(T_{pm}^2+T_c^2)}{\epsilon_p} + \frac{1}{\epsilon_c} - 1 \right]^{-1} \quad (13)$$

In equation (14), R_{ca} denotes the thermal resistance between the glass cover and the surrounding environment. This resistance is influenced by the wind heat transfer coefficient (h_w), the emissivity of the glass cover (ϵ_c), the Boltzmann constant (σ), the temperature of the glass cover (T_c), the sky temperature (T_s), and the ambient temperature (T_a).

$$R_{ca} = \left[h_w + \frac{\epsilon_c \sigma (T_c^4 - T_s^4)}{T_c} - T_a \right]^{-1} \quad (14)$$

Equation (15) is used to determine the radiation heat flux, where E_e is the flux density difference of the irradiation, J_e is the radiosity (the sum of the emitted radiation), and ∂_γ is the wavelength of the radiation.

$$Q_r = E_e - J_e = \int_0^\infty E_{e,\gamma} \partial_\gamma - \int_0^\infty J_{e,\gamma} \partial_\gamma \quad (15)$$

Equation (16) is used to determine the overall thermal efficiency (η_{th}) of the flat-plate collector with PCMs. It considers the collector's thermal efficiency (η_{th}), the overall heat transfer (Q_u) of the collector, the solar constant (G_t), and the collector area (A_c).

$$\eta_{th} = \frac{\int Q_u dt}{\int G_t A_c dt} \quad (16)$$

Equation (17) is used to determine the charging of the PCMs, where m_p is the mass of the PCMs, c_p is their specific heat capacity, T is the average temperature of the PCMs, d_t represents the diameter of the tubes, m is the mass of the working fluid, T_{out} is the output temperature, and T_{in} is the input temperature. Q_{ch} represents the charging of the PCMs, and the output efficiency of the collector is I , while A_c is the area of the collector and U_L is the overall heat loss.

$$m_p c_p \left(\frac{dT_{p,avg}}{dt} \right) + m c_p (T_{out} - T_{in}) + Q_{ch} = \eta_0 I A_c - U_L (T_{p,avg} - T_c) T_c \quad (17)$$

Equation (18) is used to determine the discharging process of the PCMs, where Q_{dis} is the discharging of the PCMs.

$$m_p c_p \left(\frac{dT_{p,avg}}{dt} \right) + m c_p (T_{out} - T_{in}) = Q_{dis} - U_L (T_{p,avg} - T_c) T_c \quad (18)$$

Equation (19) is used to determine the total heat stored by the PCMs with the addition of nanocomposite materials. A_c is the area of the collector, F_r is the fractional efficiency of the collector, G_t is the solar constant value, and U_L is the overall heat loss of the FPC. Where T_{in} is the inlet temperature, T_i is the inlet temperature in the phase change, T_{out} is the output temperature of the collector, T_p is the temperature of the plate, T_{pcm} is the temperature of the PCM, R_{tot} is the total resistance loss, and A_{pcm} depicts the area where the PCM is placed.

$$Q_u = A_c F_r [G_t \alpha_t - U_L (T_{in} - T_i)] - T_p - \frac{T_{pcm}}{R_{tot}} \times A_{pcm} \quad (19)$$

Equation (20) is used to find the overall efficiency of the PCMs during the charging and discharging processes. The efficiency of the PCM during charging is represented by η_{ch} , and the efficiency of the PCM during the discharging mode is represented by η_{dis} .

$$\eta_0 = \eta_{ch} \times \eta_{dis} \quad (20)$$

In equation (21), $E_{x,stored}$ denotes the total exergy stored within the PCM, while $E_{x,in}$ represents the total exergy entering the PCM system.

$$\eta_{ch} = \frac{E_{x,stored}}{E_{x,in}} \quad (21)$$

In equation (22), $E_{x,out}$ represents the total exergy released or discharged by the PCMs, while $E_{x,stored}$ denotes the total exergy stored within the PCMs.

$$\eta_{dis} = \frac{E_{x,out}}{E_{x,stored}} \quad (22)$$

Equation (23) determines the inlet exergy of the PCMs ($E_{x,in}$) based on their mass (m), specific heat capacity (c_p), inlet temperature (T_{in}), and outlet temperature (T_{out}), as well as the ambient temperature (T_a).

$$E_{x,in} = m c_p \left[(T_{in} - T_{out}) - T_a \ln \left(\frac{T_{in}}{T_{out}} \right) \right] \quad (23)$$

Equation (24) is used to determine the exergy out during the discharging process

$$E_{x,out} = m c_p \left[(T_{out} - T_{in}) - T_a \ln \left(\frac{T_{out}}{T_{in}} \right) \right] \quad (24)$$

Equation (25) is used to determine the total exergy of the PCMs

$$E_x = m c_p \left[(T_{in} - T_{out}) \left[1 - \frac{T_a}{T_m} \right] \right] \quad (25)$$

Equation (26) determines the exergy efficiency of the PCMs, both for simple PCMs and nanocomposite PCMs. This efficiency (η) relates the output exergy from the PCMs ($E_{x,out}$) to the input exergy ($E_{x,in}$).

$$\eta = E_{x,out} / E_{x,in} \quad (26)$$

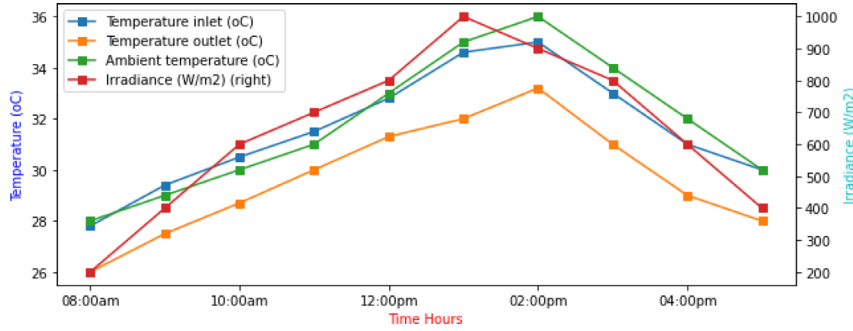


Fig. 10. Temperature and irradiance values at the inlet, outlet, and ambient conditions for the FPC.

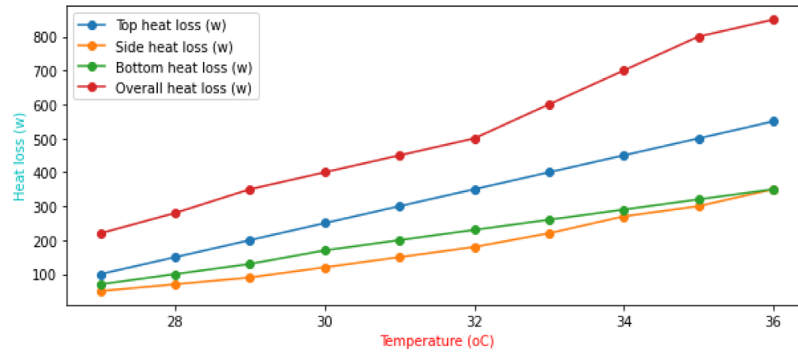


Fig. 11. Heat losses in the FPC.

4 Results

PCMs are incorporated into FPCs alongside nanocomposite materials to improve the thermal stability of energy storage. The numerical analysis includes the design aspects of heat transfer, heat loss, fluid fractions, PCM charging and discharging energy, exergy, and overall efficiency of the FPC. The collector is positioned at a latitude of 5.1679 and a longitude of 100.4783. A comparison is made between the presence of nanotubes in the proposed FPC and a conventional plain tube collector. Sodium sulfate decahydrates serve as PCM, and copper oxide is introduced to enhance the thermal stability of the PCMs.

Figure 10 illustrates the temperature variations observed in FPCs. Inlet, outlet, and ambient temperatures exhibit fluctuations throughout the day. The consistent weather conditions in Malaysia persist throughout the year. At 8:00 am, the FPC’s inlet temperature initiates at 28 °C, gradually rising throughout the day. During peak hours (1–2 pm), the inlet temperature reaches its maximum at 35 °C. Simultaneously, the outlet temperature begins at 26 °C in the morning, increasing as heat is stored and peaking at 33 °C during the same peak hours. The ambient temperature starts at 28.3 °C in the morning, reaching 36 °C at the day’s zenith. Weather data is sourced from real-time meteorological data. The irradiance value commences at 200 W/m², peaks at 1,000 W/m² during midday, subsequently decreases, and eventually returns to 200 W/m², reaching zero at sunset.

Figure 11 depicts the heat loss characteristics of the FPC, encompassing top heat loss, bottom heat loss, side heat loss, and overall heat loss. Equations (10)–(14) are used to determine the overall heat loss. The top heat loss accounts for losses in the glazing and absorber of the FPC. In the early morning, when the ambient temperature is low at 28 °C, the top heat loss is 90 W, the side loss is 50 W, the bottom loss is 70 W, and the overall heat loss is 240 W. As the day progresses and temperatures rise, the losses in the FPC escalate. At the peak temperature of 36 °C, the losses reach their maximum, with top loss at 420 W, side loss at 300 W, bottom loss at 310 W, and overall heat loss at 840 W. At sunset, the heat loss begins to decrease, paralleled by a reduction in the output of the FPC.

Figure 12 illustrates the output temperature of the working fluid released after expelling absorbed energy. Without the integration of PCMs, the output temperature is high. However, when PCMs are incorporated into the FPC, the output temperature decreases because the PCM absorbs more energy compared to a simple working fluid.

The output temperature is 28 °C without PCM, while with PCM, it is 26 °C at a working fluid flow rate of 1,500 Re. As the temperature rises, the working fluid rate is increased. At a flow rate of 3,700 Re, the output temperature without PCMs is 36 °C, and with PCMs, it is 34 °C. With a further increase in the working fluid rate, the output temperature begins to decline due to a reduction in the absorber rate. During the simulation, a high upper limit

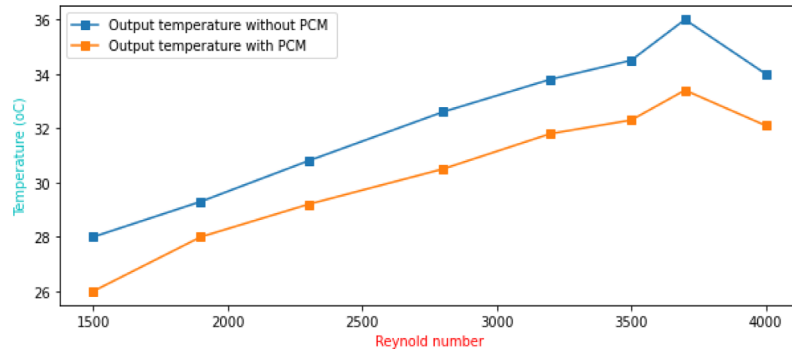


Fig. 12. Output temperature of FPC with and without integration of PCM.

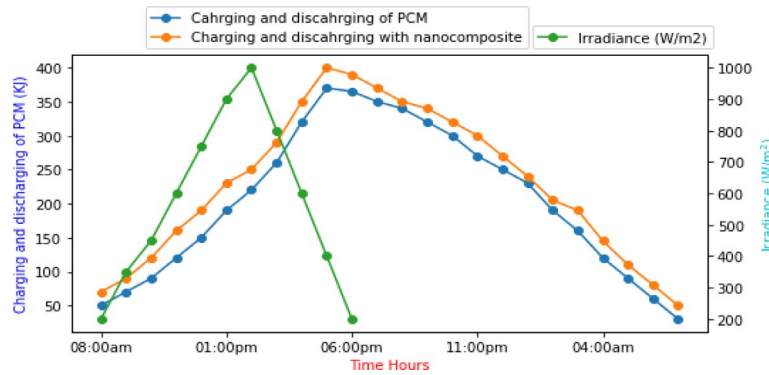


Fig. 13. Charging and discharging of PCM with and without nanocomposite materials.

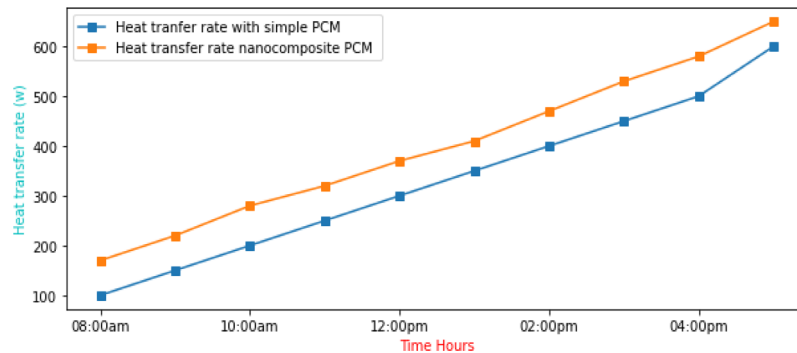


Fig. 14. Heat transfer rate of simple and nanocomposite PCM.

for the temperature value was set, leading to a peak value at a Reynolds number of 3,700. This local peak in the simulation results can be attributed to the change in heat transfer fluid viscosity as the flow transitions from laminar to turbulent.

Figure 13 illustrates the charging and discharging processes of PCM under solar radiation, comparing cases with and without the incorporation of nanocomposite materials containing sodium sulfate decahydrate. Equations (17) and (18) is used to determine the charging and discharging process of PCM. The performance of PCM during these processes is notably enhanced with the addition of nanocomposite material, particularly due to the presence

of copper oxide, which improves thermal conductivity and storage duration.

At the beginning of the day at 8:00 am, when solar radiation intensity is 100 W/m², the charging capacity of PCM without nanocomposite materials is 50 kJ, whereas with the addition of nanocomposite materials, it reaches 70 kJ. As the day progresses and solar radiation intensity increases, the storage capacity experiences a corresponding rise. During the peak hours, PCM reaches its maximum charging capacity.

By 5:00 pm, at the day’s conclusion, the charging capacity of PCM without nanocomposite materials stands at 350 kJ, while PCM with nanocomposite materials reaches

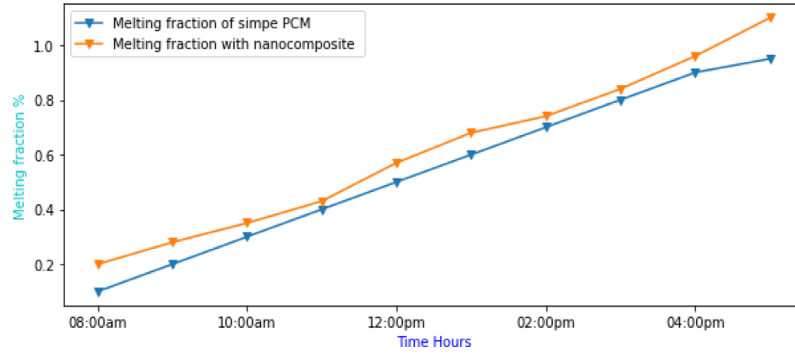


Fig. 15. Melting fraction of simple and nanocomposite PCM.

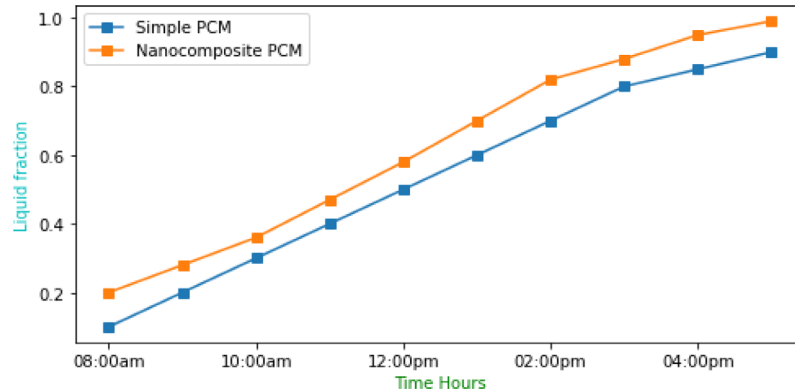


Fig. 16. Liquid fraction of simple and nanocomposite PCM.

400 kJ. In the absence of solar radiation, the stored energy is utilized to power the thermal load. Notably, during the discharging process, PCM without nanocomposite materials discharges earlier.

The highest intensity of sunlight is reached between 1 and 2 pm, allowing the FPC to operate at peak efficiency and the NePCM to charge at its maximum rate. Although the sunlight intensity decreases after this peak, the FPC continues to operate and store energy in the NePCM until the sun sets, extending the charging process until 6 PM. After sunset, the stored energy is used to power the load.

Figure 14 depicts the heat transfer rates of both simple PCM and PCM enhanced with nanocomposite materials. The heat transfer rate is significantly higher in PCM with nanocomposite materials compared to simple PCM.

At the beginning of the day, at 8:00 am, the heat transfer rate of the FPC in simple PCM is 100 W, whereas with the inclusion of nanocomposite materials in the PCMs, it reaches 160 W. Throughout the day, the heat transfer rate experiences a continuous increase. By the day's conclusion, at 5:00 pm, the heat transfer rates reach their maximum values, with simple PCM at 550 W and nanocomposite PCM at 650 W.

Figure 15 illustrates the melting fraction over time for both simple PCM and PCM enhanced with nanocomposite materials in the context of FPCs. The inclusion of sodium sulfate decahydrate allows for the absorption of heat, breaking down water molecules to store thermal energy. The

introduction of copper oxide nanocomposite materials further enhances the thermal stability of the PCM.

Starting at 8:00 am, the melting fraction of simple PCM is 0.1, while nanocomposite PCM registers a higher value of 0.2. As the day unfolds, the melting fraction rates for both materials increase. By 5:00 pm, at the day's conclusion, the melting fraction of simple PCM reaches 0.9, whereas nanocomposite PCM shows a higher value of 1.2, indicating an advanced level of thermal transformation and stability.

Figure 16 presents the liquid fraction over time for both simple PCM and PCM enhanced with nanocomposite materials. Commencing at 8:00 am, the liquid fraction for simple PCM is 0.12, while nanocomposite PCM starts at a slightly higher value of 0.2. As the day advances, the liquid fraction values for both materials increase, corresponding to an augmentation in thermal energy storage. Equation (7) is used to determine.

By 5:00 pm, at the day's conclusion, the liquid fraction for simple PCM reaches 0.90, indicating complete phase change. In contrast, the liquid fraction for nanocomposite materials is elevated to 0.99, attributed to the inclusion of metal oxide materials, signifying enhanced thermal characteristics and increased thermal energy storage capability.

Figure 17 depicts the temporal variations in exergy and mass flow rates for the FPC incorporating PCMs. Commencing at 8:00 am, the exergy rate for the FPC, devoid of PCM integration, stands at 1.2 W. However, with the

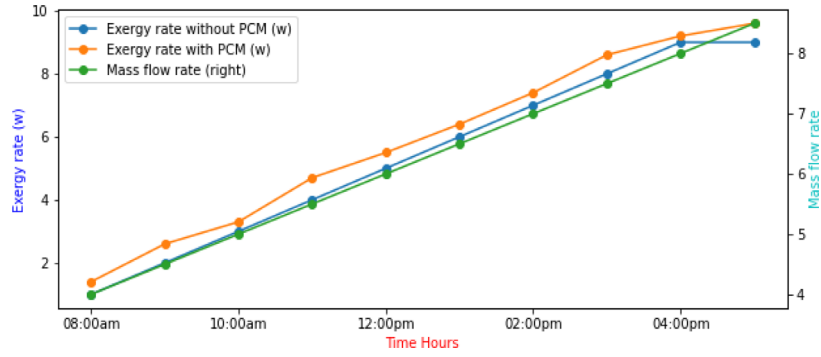


Fig. 17. Exergy rate of the FPC.

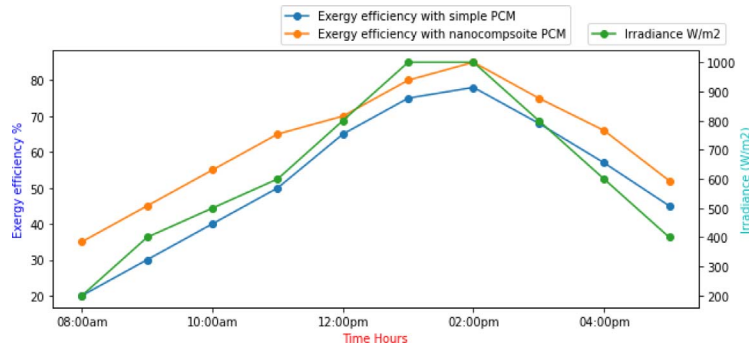


Fig. 18. Exergy efficiency of the PCMs and nanocomposite.

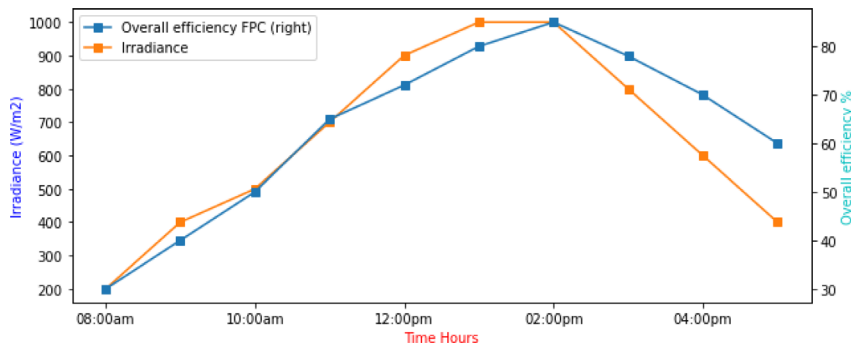


Fig. 19. Overall efficiency of the FPC concerning radiation intensity of the sun.

inclusion of phase change and nanocomposite materials, the exergy rate increases to 1.6 W, accompanied by a mass flow rate of 4. Over the course of time, both the exergy rate and mass flow rate exhibit an upward trend. At the conclusion of the observation period, the maximum exergy transfer rate is attained, reaching 10 W with the integration of PCMs and 9.2 W without such integration. Simultaneously, the mass flow rate reaches 8.5. Equations (23) and (24) is used to determine the exergy rate in and out in PCMs.

Figure 18 illustrates the exergy efficiency of the FPC with both simple PCM and nanocomposite PCMs in relation to irradiation intensity. At the commencement of the day at 8:00 am, the exergy efficiency for simple PCM stands at 20%, while for nanocomposite PCM, it is 35%, with an irradiance value of 200 W/m².

As the day progresses, the exergy efficiency experiences a corresponding increase. During the peak hours, specifically between 1:00 pm and 2:00 pm, the exergy efficiency reaches 78% for simple PCM and 85% for nanocomposite PCMs, coinciding with an irradiance intensity value of 1000 W/m². Following this peak period, as the irradiance value starts to decrease, the exergy efficiency of the FPC also exhibits a decline. Equation (26) is used to determine the overall exergy efficiency of the FPCs.

Figure 19 depicts the overall efficiency of the FPC utilizing nanotubes and nanocomposite materials in relation to sun intensity values. At sunrise, 8:00 am, the sun intensity is 200 W/m², and the collector's efficiency stands at 30%. As the day unfolds, the sun's intensity increases, leading to a corresponding rise in the collector's efficiency.

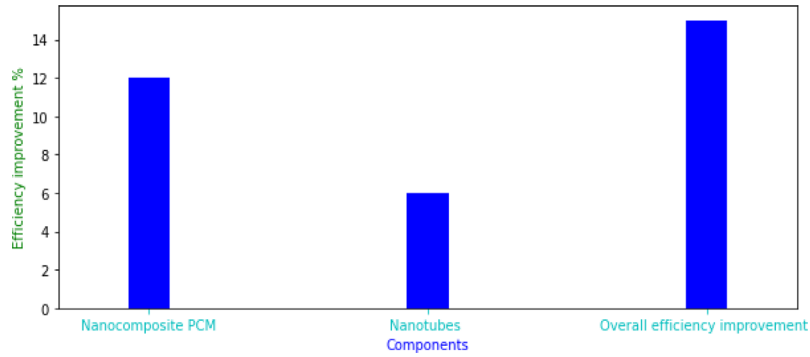


Fig. 20. FPC efficiency improvement.

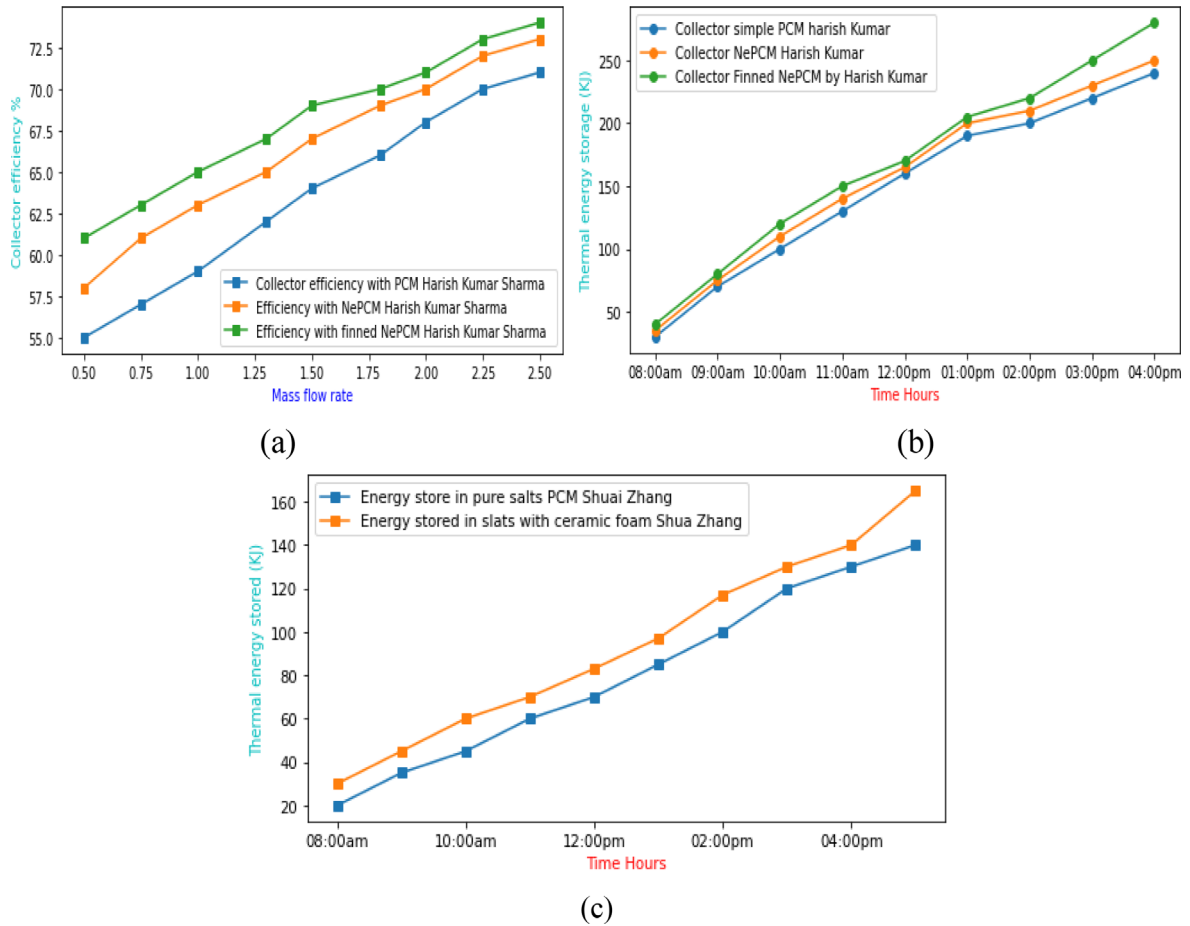


Fig. 21. Results obtained from references [11, 45] for comparison of proposed design.

During the peak hours, specifically between 1:00 pm and 2:00 pm, when the irradiance intensity reaches its zenith at $1,000 \text{ W/m}^2$, the collector achieves its highest efficiency at 85%. Post this peak period, as the sun's intensity diminishes, the efficiency of the FPC also experiences a decline.

Figure 20 illustrates the enhancement in overall efficiency in FPCs achieved through the incorporation of nanocomposite materials and nanotubes. The utilization of nanocomposite materials leads to a noteworthy 12%

improvement in the FPC's efficiency. This improvement is attributed to the enhanced thermal conductivity of PCMs facilitated by the integration of nanocomposite materials, resulting in improved efficiency in thermal energy collection and storage within the PCMs.

Simultaneously, the use of nanotubes contributes to a 6% increase in the efficiency of the FPC. When both nanocomposite materials and nanotubes are employed, the combined effect results in an overall efficiency improvement of 15% in the FPC.

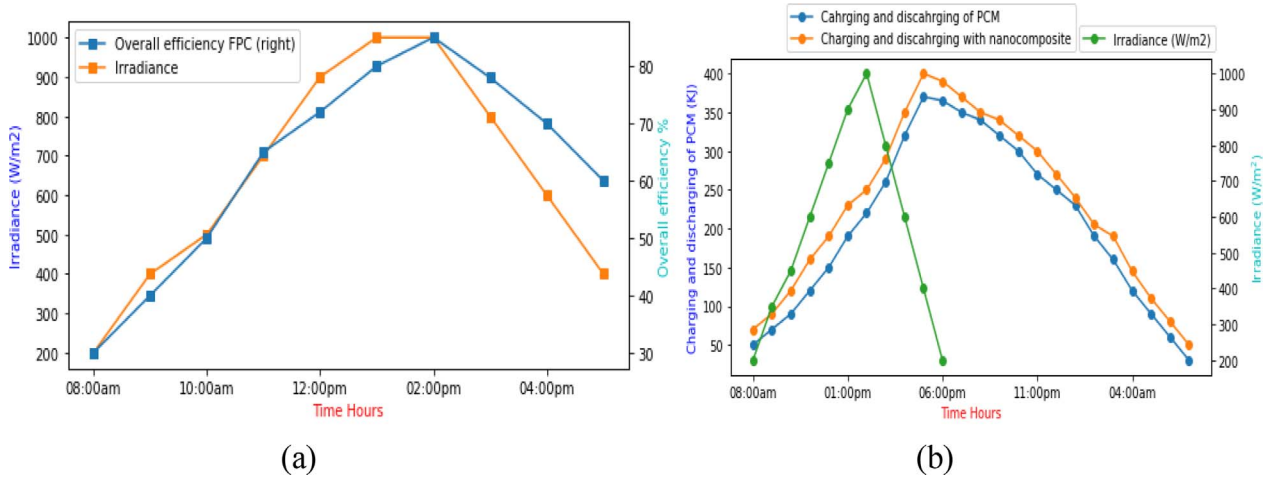


Fig. 22. Proposed design results for comparison.

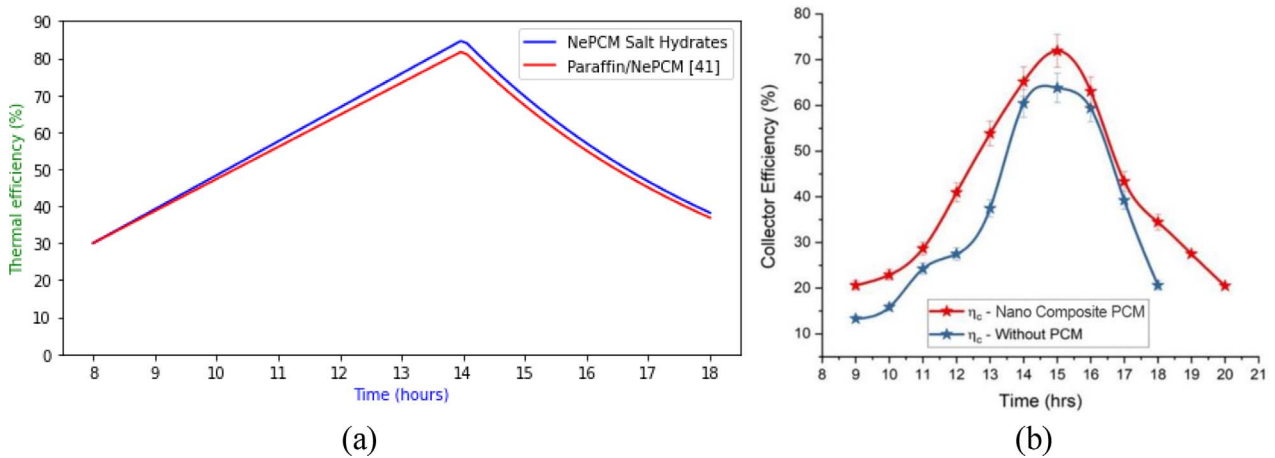


Fig. 23. (a) FPC efficiency comparison with the work from [46] (b) FPC with HnPCM and without PCM [47].

4.1 Comparison of results

In Figure 21, the outcomes of Harish Kumar Sharma and Shuai Zhang are depicted, showcasing the integration of PCMs with FPCs [11, 45]. Figure 21a reveals Harish Kumar's utilization of Nano-enhanced PCM and finned PCM to enhance FPC efficiency with respect to mass fraction. NePCM, consisting of nano paraffin wax and graphene, demonstrates an efficiency of 72.5%, while efficiency improves to 74% with finned NePCM, and simple PCM achieves 70%.

Figure 21b illustrates the thermal energy storage characteristics of these phase-change materials. Simple PCM exhibits thermal energy storage of 200 kJ, whereas NePCM enhances it to 250 kJ, and finned NePCM further increases the storage to 270 kJ.

In Figure 21c, the results from Shuai Zhang's study are presented, featuring a design incorporating pure salt and the addition of ceramic foam to augment collector efficiency and extend thermal energy storage duration [45]. The use of pure molten salt yields an energy storage capacity of 140 kJ,

while the incorporation of ceramic foam enhances this capacity to 170 kJ.

In Figure 22, the outcomes of the suggested design are illustrated, encompassing the overall efficiency of the FPC integrated with Nano-Enhanced PCM and the corresponding charging and discharging times of the PCMs.

Figure 22a depicts the overall efficiency of the FPC with the inclusion of sodium sulfate decahydrate and copper oxide. The integration of the FPC with nanotubes for PCM storage leads to an impressive 85% enhancement in overall efficiency.

Figure 22b showcases the charging and discharging processes of the PCMs, demonstrating superior performance compared to the approaches of Harish Kumar and Shuai Zhang [11, 45].

4.2 Practical comparison of FPC with NePCM

Figure 23a demonstrates the practicality of integrating an FPC with NePCM to enhance its thermal performance. According to reference [46], the thermal efficiency of a

collector using paraffin wax NePCM reaches 82% at 2 pm. In contrast, the collector in this study, which utilizes sodium sulfate decahydrate and copper oxide, achieves an efficiency of 85% at the same time. This shows that the thermal efficiency in this work surpasses that of the compared study.

Figure 23b depicts the experimental comparison of the thermal efficiency of the FPC with HnPCM and without PCM. The efficiency of the FPC without HnPCM is 63.8%, and with the addition of HnPCM, the efficiency improves to 71.93%.

4.3 Limitation

NePCM improves energy storage performance and enhances the efficiency of FPCs when integrated with them. Incorporating NePCM into an FPC reduces load fluctuations and conserves energy. Salt hydrates combined with metal oxide-based phase change materials enhance storage duration and performance, although NePCM have certain limitations. The thermal conductivity of salt hydrate PCM is low, and the preparation of NePCM involves chemical and physical processes that are harmful to the environment. Additionally, the inclusion of nanomaterials in PCM is expensive, driving up the cost of NePCM. Selecting appropriate materials for NePCM preparation is also challenging; if suitable materials are unavailable, it can lead to instability in the NePCM. Moreover, the high leakage rate of inorganic phase change materials negatively impacts the performance of the FPC.

5 Conclusion

Thermal energy storage not only meets energy demands but also reduces the burden on renewable energy resources. PCM are particularly effective for storing thermal energy because of their high heat of fusion and excellent thermal conductivity. These materials absorb thermal energy, causing their molecules to break apart and transition from a solid to a liquid state, thus storing the energy efficiently. In this design, FPCs are integrated with PCMs to store thermal energy. Sodium sulfate decahydrate is used as the PCM for energy storage in this setup. To enhance thermal conductivity and improve storage efficiency, a copper oxide-based nanocomposite material is added to the salt. The PCMs and the energy they store are contained within nanotubes in the FPC. The key findings of the work include:

- The incorporation of nanocomposites with PCMs results in a 12% increase in efficiency, while the use of nanotubes contributes an additional 6% improvement, leading to an overall improvement of 15%. Consequently, the overall efficiency of the FPC in this design reaches 85%.
- With the use of sodium sulfate decahydrate, copper oxide, and nanotubes as a NePCM, the exergy efficiency of the FPC also improves by 85%.
- The charging and discharging of the NePCM are more efficient compared to simple PCM. The NePCM stores 50 kJ more energy than the simple PCM.

- The liquid fraction of the simple PCM is 0.90, whereas in this work, the NePCM achieves a liquid fraction of 0.99, demonstrating a significant improvement over the simple PCM.
- The flow rate is maintained within the range of 1,500–4,000 Reynolds numbers.

System simulation is conducted using Anaconda Jupyter Notebook with Python language. For future work, exploring various types of nanocomposite materials to further enhance thermal conductivity and extend thermal energy storage duration in PCMs is recommended. Additionally, implementing a rotating absorber pipe could be considered to enhance the efficiency of the FPC even further.

Funding

The research work is financially supported by the Universiti Sains Malaysia Short-Term Grant 304/PELECT/6315747.

Conflicts of interest

The authors declare that they have no known competing financial interests or personal relationships that could have appeared to influence the work reported in this paper.

References

- 1 Khan M.M.A., Ibrahim N.I., Mahbulul I.M., Ali H.M., Saidur R., Al-Sulaiman F.A. (2018) Evaluation of solar collector designs with integrated latent heat thermal energy storage: A review, *Sol. Energy* **166**, 334–350.
- 2 Sakhaei S.A., Valipour M.S. (2021) Thermal behavior of a flat plate solar collector with simultaneous use of helically heat collecting tubes and phase change materials. *Sust. Energy Technol. Assess.* **46**, 101279.
- 3 Mehrdad S., Mirkhani N., Sajadi B. (2018) A comprehensive study on the effect of hot water demand and PCM integration on the performance of SDHW system, *Sol Energy* **159**, 405–414.
- 4 Pere M., Solé C., Castell A., Cabeza L.F. (2014) The use of phase change materials in domestic heat pump and air-conditioning systems for short term storage: A review, *Renew. Sust. Energy Rev.* **39**, 1–13.
- 5 Luisa C.F., Manuel I., Cristian S., Joan R., Miquel N. (2006) Experimentation with a water tank including a PCM module, *Sol. Energ. Mat. Sol. Cells* **90**, 9, 1273–1282.
- 6 Hirmiz R., Lightstone M.F., Cotton J.S. (2018) Performance enhancement of solar absorption cooling systems using thermal energy storage with phase change materials, *Appl. Energy* **223**, 11–29.
- 7 Mohamed E.Z., Zhao J., Ammar H.E., Yanping D., Hammad F.A., Ling M., Kabeel A.E., Sadek S. (2019) Performance augmentation of flat plate solar water collector using using phase change materials and nanocomposite phase change materials: A review, *Process Saf. Environ. Prot.* **128**, 135–157.
- 8 Radouane E. (2021) Improvement of the thermal performance of a solar triple concentric-tube thermal energy storage unit using cascaded phase change materials, *J. Energ. Storage* **42**, 103047.

- 9 Seyed S.A., Valipour M.S. (2021) Thermal behavior of a flat plate solar collector with simultaneous use of helically heat collecting tubes and phase change materials, *Sust. Energ. Technol. Assess.* **46**, 101279.
- 10 Radouane E., Qarnia H.E. (2019) Performance evaluation of a solar thermal energy storage system using nanoparticle-enhanced phase change material, *Int. J. Hydrogen Energy* **44**, 3, 2013–2028.
- 11 Sharma H.K., Kumar S., Kumar S., Verma S.K. (2022) Performance investigation of flat plate solar collector with nanoparticle enhanced integrated thermal energy storage system, *J. Energ. Storage* **55**, 105681.
- 12 Sinem I., Yıldız C. (2020) Improving thermal energy storage efficiency of solar collector tanks by placing phase change materials in novel finned-type cells, *Ther. Sci. Eng. Prog.* **19**, 100618.
- 13 Fei L., Zhang Y., Liu Q., Jin Z., Zhao X., Long E. (2017) Experimental study on thermal energy storage performance of water tank with phase change materials in solar heating system, *Proc Eng.* **205**, 3027–3034.
- 14 Wang D., Huo X., Liu Y., Chen Y., Fan B., Xu T., Wang L. L. (2022) A study on frost and high-temperature resistance performance of supercooled phase change material-based flat panel solar collector, *Sol. Energ. Mat. Sol. Cells* **239**, 111665.
- 15 Greg W., Rubel R.I. (2021) Design improvement of a laboratory prototype for efficiency evaluation of solar thermal water heating system using phase change material (PCMs), *Results Eng.* **12**, 100301.
- 16 Abu-Hamdeh N.H., Khoshaim A., Alzahrani M.A., Hatamleh R.I. (2022) Study of the flat plate solar collector's efficiency for sustainable and renewable energy management in a building by a phase change material: Containing paraffin-wax/Graphene and Paraffin-wax/graphene oxide carbon-based fluids, *J. Build. Eng.* **57**, 104804.
- 17 Gul H., Ghafoor M.A., Yousaf M., Imran M., Zaman M., Elkamel A., Haq A., Rizwan M., Wilberforce T., Abdelkareem M.A., Olabi A.G. (2022) Low temperature phase change materials for thermal energy storage: Current status and computational perspectives, *Sust. Energ. Technol. Assess.* **50**, 101808.
- 18 Debasree G., Ghose J., Datta P., Kumari P., Paul S. (2022) Strategies for phase change material application in latent heat thermal energy storage enhancement: Status and prospect, *J. Energ. Storage* **53**, 105179.
- 19 Maridurai T., Rajkumar S., Arunkumar M., Mohanavel V., Arul K., Madhesh D., Subbiah R. (2022) Performance study on phase change material integrated solar still coupled with solar collector, *Mat. Today: Proc.* **59**, 1319–1323.
- 20 Arvind Kumar S., Agarwal N., Saxena A. (2021) Effect of extended geometry filled with and without phase change material on the thermal performance of solar air heater, *J. Energ. Storage* **39**, 102627.
- 21 Ali S., Farahani S.D., Alizadeh A. (2023) Numerical investigation and group method of data handling-based prediction on new flat plate solar collector integrated with nanoparticles enhanced phase change materials and tube rotation mechanism, *J. Energ. Storage* **67**, 107542.
- 22 Ahmed S.F., Rafa N., Mehnaz T., Ahmed B., Islam N., Mofijur M., Hoang A.T., Shafiqullah G.M. (2022) Integration of phase change materials in improving the performance of heating, cooling, and clean energy storage systems: An overview, *J. Cleaner Prod.* **364**, 132639.
- 23 Wang C., Chen K., Huang J., Cai Z., Hu Z., Wang T. (2019) Thermal behavior of polyethylene glycol based phase change materials for thermal energy storage with multiwall carbon nanotubes additives, *Energy* **180**, 873–880.
- 24 Xin L., Zhao Y., Min X., Xiao J., Wu X., Mi R., Liu Y., Huang Z., Fang M. (2022) Carbon nanotubes modified graphene hybrid Aerogel-based composite phase change materials for efficient thermal storage, *Energ. Build.* **273**, 112384.
- 25 Muhammad Z.H., Jin X., Sharma R., Pei J., Hu J.W. (2022) Enhancing the compressive strength of thermal energy storage concrete containing a low-temperature phase change material using silica fume and multiwalled carbon nanotubes, *Constr. Build. Mat.* **314**, 125659.
- 26 NematpourKeshetli A., Iasiello M., Langella G., Bianco N. (2023) Increasing melting and solidification performances of a phase change material-based flat plate solar collector equipped with metal foams, nanoparticles, and wavy wall-Y-shaped surface, *Energy Convers. Manag.* **291**, 117268.
- 27 NematpourKeshetli A., Iasiello M., Langella G., Bianco N. (2023) Thermal enhancement techniques for a lobed-double pipe PCM thermal storage system, *Appl. Thermal Eng.* **233**, 121139.
- 28 Abdulateef A.M., Mat S., Abdulateef J., Sopian K., Al-Abidi A.A. (2018) Thermal performance enhancement of triplex tube latent thermal storage using fins-nano-phase change material technique, *Heat Transf. Eng.* **39**, 12, 1067–1080.
- 29 Shehram M., Javid T., Khalid Z. (2021) Hybrid multijunction PV and CST based solar cooling system using flat plate collector and graphene based nanofluid, in: *2021 6th International Electrical and Electronics Engineering Conference (IEEC, April 2021)*.
- 30 Jamil M.M., Sidik N.A.C., Umar U.S., Hamisu M.T., Sa'ad A. (2019) Carbon nanotube for solar energy applications: A review, *J. Adv. Res. Fluid Mech. Therm. Sci.* **56**, 2, 233–247.
- 31 Christina V.P., Kartsonakis I.A., Charitidis C.A. (2021) Towards phase change materials for thermal energy storage: Classification, improvements and applications in the building sector, *Appl. Sci.* **11**, 41490.
- 32 Nazir H., Batool M., Bolivar Osorio F.J., Isaza-Ruiz M., Xu X., Vignarooban K., Phelan P., Kamman A.M. (2019) Recent developments in phase change materials for energy storage applications: A review, *Int. J. Heat Mass Transf.* **129**, 491–523.
- 33 Muhammad F.J., Rehman Z., Čekon M., Čurpek J., Farooq R., Cui H., Khan I. (2021) Inorganic phase change materials in thermal energy storage: A review on perspectives and technological advances in building applications, *Energ. Build.* **252**, 111443.
- 34 Mohamed S.A., Al-Sulaiman F.A., Ibrahim N.I., Zahir M.H., Al-Ahmed A., Saidur R., Yılbaş B.S., Sahin A.Z. (2017) A review on current status and challenges of inorganic phase change materials for thermal energy storage systems, *Renew. Sust. Energ. Rev.* **70**, 1072–1089.
- 35 Teamah H.M., Teamah M. (2022) Integration of PCM in flat plate solar water collector: A state of the art, opportunities, and challenges, *J. Energ. Storage* **54**, 105357.
- 36 Gholamabbas S., Mehrali M., Shahi M., Brem G., Mahmoudi A. (2022) Progress of experimental studies on compact integrated solar collector-storage retrofits adopting phase change materials, *Sol. Energ.* **237**, 62–95.
- 37 Faraj K., Khaled M., Faraj J., Hachem F., Castelain C. (2020) Phase change materials thermal energy storage systems for cooling applications in buildings: A review. *Renew. Sust. Energ. Rev.* **119**, 109579.

- 38 Amaral C., Vicente R., Marques P.A.A.P., Barros-Timmons A. (2017) Phase change materials and carbon nanostructures for thermal energy storage: A literature review. *Renew. Sust. Energ. Rev.* **79**, 1212–1228.
- 39 Amidu M.A., Addad Y., Riahi M.K., Abu-Nada E. (2021) Numerical investigation of nanoparticles slip mechanisms impact on the natural convection heat transfer characteristics of nanofluids in an enclosure, *Sci. Rep.* **11**, 1, 15678.
- 40 Amidu M.A., Ali M., Alkaabi A.K., Addad Y. (2023) A critical assessment of nanoparticles enhanced phase change materials (NePCMs) for latent heat energy storage applications, *Sci. Rep.* **13**, 17829.
- 41 Mashhour A.A., Mohammed A., Mohammad R.S. (2022) Effects of various types of nanomaterials on PCM melting process in a thermal energy storage system for solar cooling application using CFD and MCMC methods, *Int. J. Heat Mass Transf.* **195**, 123204.
- 42 Badieli Z., Eslami M., Jafarpur K. (2020) Performance improvements in solar flat plate collectors by integrating with phase change materials and fins: A CFD modeling, *Energy* **192**, 116719.
- 43 Mahfuja A.K., Yan L., Khalesi J., Sarunac N., Romero C. (2024) Energy and exergy analysis of a laboratory-scale latent heat thermal energy storage (LTES) using salt-hydrate in a staggered tube arrangement, *J. Energ. Storage* **87**, 111320.
- 44 Badieli Z., Eslami M., Jafarpur K. (2020) Performance improvements in solar flat plate collectors by integrating with phase change materials and fins: A CFD modeling, *Energy* **192**, 116719.
- 45 Zhang S., Yan Y. (2023) Energy, exergy and economic analysis of ceramic foam-enhanced molten salt as phase change material for medium-and high-temperature thermal energy storage, *Energy* **262**, 125462.
- 46 Poongavanam G.K., Vigneswaran V.S., Murugan P., Cheralthan M., Velraj R., Kim S.C., Ramkumar V. (2024) Exploring the thermal performance of a solar air heater with a V-corrugated and shot-blasted absorber plate comprising nano-enhanced phase change materials, *J. Energ Storage* **77**, 109955.
- 47 Bharathiraja R., Ramkumar T., Selvakumar M., Sasikumar K. (2014) Experimental and numerical analysis of hybrid nano-enhanced phase change material (PCM) based flat plate solar collector, *J. Energ. Storage* **96**, 112649.